ELSEVIER

Journal of Power Sources 108 (2002) 117–127

JOURNAL OF POWER SOURCES

www.elsevier.com/locate/jpowsour

Annealing effects on the physicochemical characteristics of hydrous ruthenium and ruthenium–iridium oxides for electrochemical supercapacitors

Chi-Chang Hu*, Yao-Huang Huang, Kwang-Huei Chang

Department of Chemical Engineering, National Chung Cheng University, Chia-Yi 621, Taiwan, ROC

Received 12 March 2001; received in revised form 14 May 2001; accepted 19 December 2001

Abstract

The electrochemical (EC) properties and stability of hydrous ruthenium oxide (denoted as $RuO_x{\cdot}nH_2O$) and ruthenium–iridium oxide (denoted as $(Ru + Ir)O_y{\cdot}mH_2O$) were systematically investigated in 0.5 M H_2SO_4 by cyclic voltammetry (CV) and chronopotentiometry (CP). The EC characteristics of $RuO_x{\cdot}nH_2O$ and $(Ru + Ir)O_y{\cdot}mH_2O$ annealed at temperatures equal to/above 200 °C were demonstrated to be more applicable for the EC supercapacitors. The crystalline information of these oxides annealed in air for 2 h up to 300 °C was obtained from the X-ray diffraction (XRD) spectra. The morphologies of these oxide-coated electrodes were examined by a scanning electron microscope (SEM). The effect of annealing temperatures on the surface composition of $(Ru + Ir)O_y{\cdot}mH_2O$ was studied by X-ray photoelectron spectroscopy (XPS).

Keywords: Hydrous Ru and Ru–Ir oxides; Annealing; Electrochemical characteristics; EC supercapacitor

1. Introduction

As a result of the unique pulse-power density of supercapacitors, the electrochemical (EC) and textural characteristics of electrode materials for this device have attracted much interest of electrochemists [1–8]. In addition, the energy density of EC supercapacitors based on a combination of faradaic pseudocapacitance and double-layer capacitance should be higher than that of double-layer supercapacitors [4,5]. Accordingly, transition metal oxides and conducting polymers with several oxidation states/structures [1–4,8] are considered as the most promising materials applicable in EC supercapacitors. Since the double-layer charging–discharging process is considered to be indefinitely reversible, the performance of an EC supercapacitor is mainly determined by the EC characteristics of the electrode materials [1–4,8]. Fundamental understandings of the EC and textural characteristics of various electroactive materials are therefore very important for the practical usage of EC supercapacitors.

Hydrous ruthenium oxide has been reported to be the most promising material for the EC supercapacitor [1,2,5]. The preparation and characterization of this material on a ruthenium metal have been systematically investigated by Hadzi-Jordanov et al. [9], which showed excellent pseudocapacitive characteristics. The $RuO_2{\cdot}nH_2O$ powders with an amorphous structure fabricated by a sol–gel process were found to exhibit very high specific capacitance while the preparation steps of this process are relatively complicated and uneasily controlled [5]. Recently, a novel method via only one step (i.e. CV) in preparing hydrous ruthenium ($RuO_x{\cdot}nH_2O$) and ruthenium–iridium oxides ($(Ru + Ir)O_y{\cdot}mH_2O$) has been developed [1,2] to replace the sol–gel process. In addition, the specific capacitance of $RuO_x{\cdot}nH_2O$ was sharply promoted by the intercalation of iridium oxide into the $RuO_x{\cdot}nH_2O$ matrix, due to the increase in nonstoichiometric electroactive sites [2]. However, the freshly prepared $RuO_x{\cdot}nH_2O$ and $(Ru + Ir)O_y{\cdot}mH_2O$ deposits were found to be unstable after several cycles of charging–discharging in H_2SO_4 although their EC reversibility was very high [2]. Accordingly, treatments improving stability and remaining highly EC reversibility of these hydrous oxides have to be carried out to insure their good performance.

The purpose of this work is to investigate effects of the annealing temperature on the textural properties of $RuO_x{\cdot}nH_2O$ and $(Ru + Ir)O_y{\cdot}mH_2O$ deposits, including crystalline, morphological and compositional information. The EC characteristics of $RuO_x{\cdot}nH_2O$ and $(Ru + Ir)O_y{\cdot}mH_2O$ were

* Corresponding author. Tel.: +886-5272-0411; fax: +886-5272-1206.
E-mail address: chmhcc@ccunix.ccu.edu.tw (C.-C. Hu).

0378-7753/02/$ – see front matter
PII: S0378-7753(02)00011-3

evaluated by both CV and CP. The relationships between textural and EC properties of these oxide deposits with annealing were systematically integrated for the application of EC supercapacitors.

2. Experimental

The preparation procedure of $RuO_x{\cdot}nH_2O$ and $(Ru + Ir)O_y{\cdot}mH_2O$ is similar to that reported in [1,2]. Hydrous oxide deposits were directly deposited onto commercial 99% titanium substrates (10 mm × 10 mm × 2 mm) by CV. Prior to voltammetric deposition, these substrates were mechanically polished by emery particles blown by a high-pressure air compressor. Then, they were degreased with soap and water and etched in a 6 M HCl solution at ca. 90 °C for 1.5 h. They were rinsed with water again and pickled in a solution consisting of DMF (*N*,*N*-dimethylformamide, Wako E.P., Japan) water and HF (Wako E.P., Japan) in the volume ratio 40:7.5:2.5 for 10 min. After pickling, the substrates were rinsed with acetone and water, coated with PTFE films and then placed in the deposition solution. The exposed surface area of these substrates is equal to 1 cm^2. The initial pH value of deposition baths was kept at 2.0, which were consisted of 0.01 M HCl and 0.1 M KCl with 5 mM $RuCl_3{\cdot}xH_2O$ (Johnson Matthey) (and 1 mM $IrCl_3{\cdot}xH_2O$ for the binary oxide (Johnson Matthey)). The EC deposition of hydrous oxide deposits was induced via CV between −0.2 and 1.0 V at 50 °C for 120 cycles. After deposition, the PTFE films were removed from the electrodes and then these electrodes were rinsed with pure water to remove the residual deposition solution. Then, they were dried in an oven at room temperature (ca. 25 °C) and a pressure of 400 mmHg. For EC studies, the oxide-coated electrodes were doubly coated with epoxy resin and PTFE films, which have exposed geometric surface areas equal to 1 cm^2.

Cyclic voltammetry for depositing $RuO_x{\cdot}nH_2O$ and $(Ru + Ir)O_y{\cdot}mH_2O$ was performed by an EC analyzer system, BAS 100W (Bioanalytic system Inc., USA). Another EC analysis system, a model CHI 633A (CH Ins. Co, USA) was employed to perform the EC characterization using chronopotentiometry and CV. All experiments were carried out in a three-compartment cell. An Ag/AgCl electrode (Argenthal, 3 M KCl, 0.207 V versus SHE at 25 °C) was used as the reference electrode meanwhile a platinum wire with an exposed geometric area equal to 5 cm^2 was employed as the counter electrode. Note that the voltammetric responses of these oxide deposits were not affected by a change in exposed geometric surface areas, varying from 5 to 20 cm^2, for the counter electrodes. A Luggin capillary, whose tip was set at a distance of 1–2 mm from the surface of working electrodes, was used to minimize errors due to *i*R drop in the electrolytes.

For textural analysis, the electrodes were employed without any further treatments. X-ray diffraction (XRD) analysis (Rigaku X-ray diffractometer using a Cu target) was employed to obtain crystalline information of the deposits with annealing. Surface morphologies of these deposits were examined by a scanning electron microscope (SEM JEOL JSM 35). Surface composition of $(Ru + Ir)O_y{\cdot}mH_2O$ with annealing was examined by X-ray photoelectron spectroscopic (XPS) measurements that were performed with an ESCA 210 (VG Scientific Ltd.) spectrometer. XPS spectra employed Mg Kα ($h\nu = 1253.6$ eV) irradiation as the photosource, with a primary voltage of 12 kV and an emission current 17 mA. The analysis chamber pressure during scans was approximately 10^{-10} mbar. The average oxide loading of $RuO_x{\cdot}nH_2O$ and $(Ru + Ir)O_y{\cdot}mH_2O$ measured by the weight difference between the substrate and the oxide-coated electrode through means of a microbalance (Sartorius BP 211D, Germany) was 9.4×10^{-4} and 4.5×10^{-4} g, respectively.

All solutions used in this work were prepared with 18 MΩ cm water produced by a reagent water system (MILLI-Q SP, Japan) and all reagents not otherwise specified in this work were Merck, GR. In addition, the aqueous solution, containing 0.5 mol dm^{-3} H_2SO_4, employed to study the EC behavior of $RuO_x{\cdot}nH_2O$ and $(Ru + Ir)O_y{\cdot}mH_2O$ was degassed with purified nitrogen gas before voltammetric measurements meanwhile a nitrogen blanket was used during the measurements. The solution temperature (unless otherwise specified) was maintained at 25 °C by means of a water thermostat (HAAKE DC3 and K20).

3. Results and discussion

3.1. Textural characteristics

The crystalline information of both $RuO_x{\cdot}nH_2O$ and $(Ru + Ir)O_y{\cdot}mH_2O$ deposits with annealing at various temperatures is systematically compared in this work. Typical results for the $RuO_x{\cdot}nH_2O$ and $(Ru + Ir)O_y{\cdot}mH_2O$ deposits annealed at 100, 150, 200, 250 and 300 °C are shown as patterns 2–6 in Fig. 1a and b, respectively. In addition, the XRD patterns for the as-prepared oxides are also shown as curve 1 in the same figures, respectively. On curve 1 in Fig. 1a, there exist Ti and Ru diffraction peaks on the as-prepared deposit although the oxidation states of main surface ruthenium species on this deposit evidenced by XPS were Ru(IV) and Ru(VI) [1]. With the above results in mind, the as-prepared $RuO_x{\cdot}nH_2O$ film is inferred to consist of a mixture of Ru(0), Ru(II), Ru(IV) and Ru(VI) species. Note that a comparison of curves 1–6 reveals two facts. First, diffraction peaks corresponding to RuO_2 are found at annealing temperature equal to or above 100 °C. This result indicates that dehydration of $RuO_x{\cdot}nH_2O$ should favor the formation of crystalline RuO_2. Second, ruthenium metal within $RuO_x{\cdot}nH_2O$ deposits has been oxidized to RuO_2 significantly at annealing temperatures equal to 200 °C since at this temperature, the intensity of diffraction peaks corresponding to ruthenium obviously decreased and these peaks disappeared

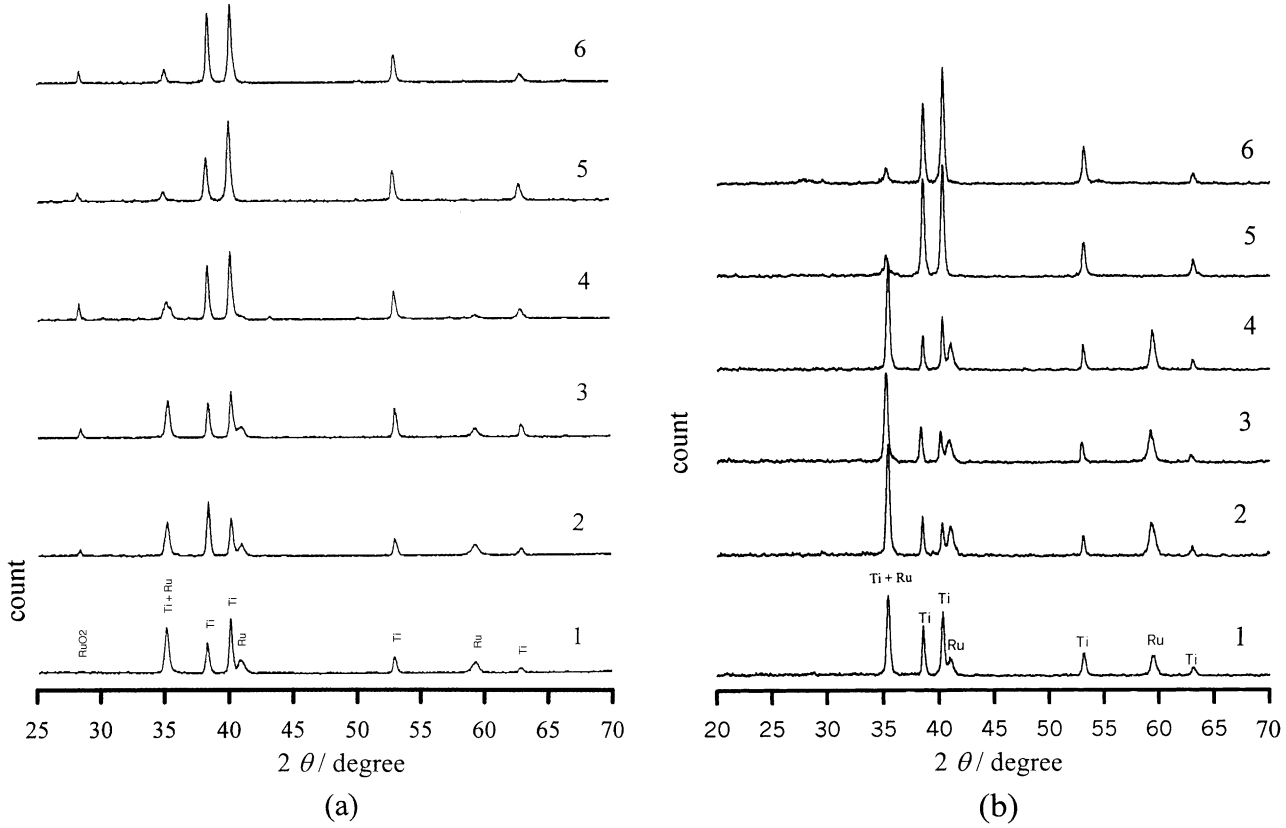

Fig. 1. XRD spectra for (a) $RuO_x{\cdot}nH_2O$ and (b) $(Ru + Ir)O_y{\cdot}mH_2O$ annealed at (1) 25; (2) 100; (3) 150; (4) 200; (5) 250 and (6) 300 °C.

at annealing temperatures equal to or above 250 °C. From the above results and discussion, the $RuO_x{\cdot}nH_2O$ deposits fabricated by CV with annealing in air for 2 h at temperatures equal to or above 200 °C should be mainly consisted of crystalline RuO_2.

A comparison of curves 1 in Fig. 1a and b reveals that the main diffraction peaks on both deposits are the same, indicating that the major electroactive species on both $RuO_x{\cdot}nH_2O$ and $(Ru + Ir)O_y{\cdot}mH_2O$ deposits should be ruthenium oxide although iridium oxide was demonstrated to present in the binary oxide deposit. In addition, a comparison on curves 4 in both figures, the diffraction intensities of ruthenium peaks on the binary oxide deposit were not significantly degraded by the annealing treatment at a temperature of 200 °C while an opposite phenomenon was found for the $RuO_x{\cdot}nH_2O$ deposit. On the other hand, all diffraction peaks corresponding to ruthenium disappeared on both deposits at temperature equal to 250 °C (Fig. 1a and b). The above difference is attributable to the presence of iridium oxide within the $RuO_x{\cdot}nH_2O$ matrix, enlarging the activation energy for the formation of RuO_2 due to their different lattice constants. This opinion is further supported by the absence of any diffraction peak of RuO_2 on the $(Ru + Ir)O_y{\cdot}mH_2O$ deposit at annealing temperature equal to or above 100 °C.

Typical SEM photographs for $RuO_x{\cdot}nH_2O$ deposits with annealing at 100 and 200 °C are shown in Fig. 2(a,b) and 2(c,d), respectively. In addition, the SEM photographs for $(Ru + Ir)O_y{\cdot}mH_2O$ deposits with annealing at 100 and 200 °C are shown in Fig. 2(e,f) and 2(g,h), respectively. Note in Fig. 2a–d that $RuO_x{\cdot}nH_2O$ has a spherical morphology with a very rough property. In addition, the vaporization of water molecules renders the cracking of these deposits while the surface of spherical grains (very small grains in Fig. 2b and d) became smoother at a higher annealing temperature. From a comparison of Fig. 2(a and b), and (e and f) the size of $(Ru + Ir)O_y{\cdot}mH_2O$ particles is much smaller (about 150–300 nm) than that of $RuO_x{\cdot}nH_2O$ (ca. 1–1.5 μm) meanwhile a more porous surface is found on the former deposit. In addition, the morphology of this deposit is very similar to the outward appearance of a etched titanium substrate [10], indicating that the $(Ru + Ir)O_y{\cdot}mH_2O$ particles prefer to grow on the edges of etched pores. The above phenomenon is attributable to a higher current density of oxide deposition distributed on the pore edges, favoring the nucleation and deposition of $(Ru + Ir)O_y{\cdot}mH_2O$ particles. The nucleation and deposition of $RuO_x{\cdot}nH_2O$ are believed to behave similarly. From a comparison of Fig. 2(e–h), the $(Ru + Ir)O_y{\cdot}mH_2O$ particles became denser and larger (about 300–400 nm) with the annealing temperature changed from 100 to 200 °C while its porous nature remained. This result implies a reconstruction of $(Ru + Ir)O_y{\cdot}mH_2O$ particles due to the movement of surface Ru/Ir oxides with a lower coordination number into the energy-favorable sites.

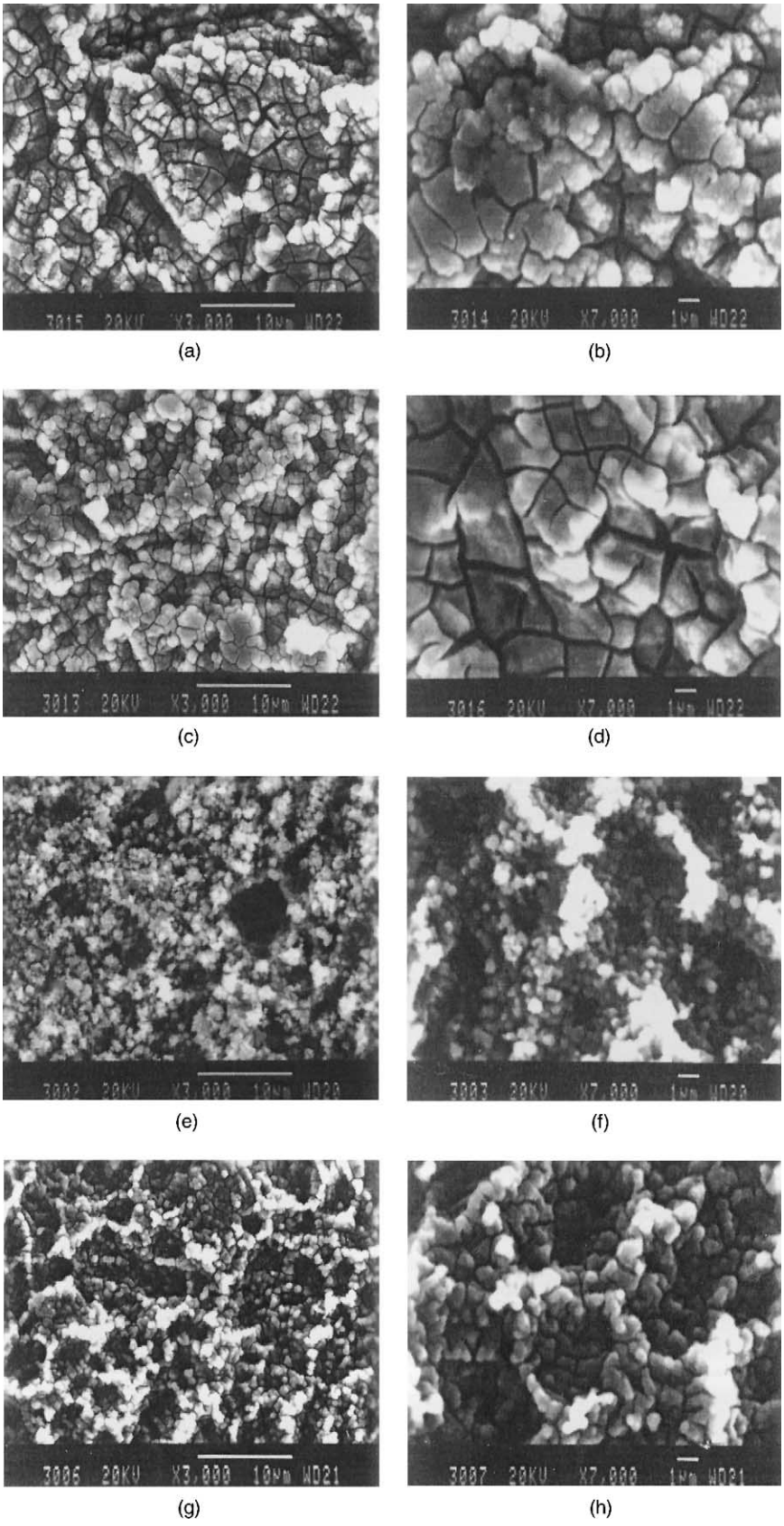

Fig. 2. SEM photographs for $RuO_x{\cdot}nH_2O$ with annealing at (a and b) 100, and (c and d) 200 °C; for $(Ru + Ir)O_y{\cdot}mH_2O$ with annealing at (e and f) 100 and (g and h) 200 °C.

The activation energy of the movement of surface atoms from a metastable state to a more stable state should be overcome by the annealing treatment since no obvious change in morphologies of the $(Ru + Ir)O_y{\cdot}mH_2O$ particles was found when the annealing temperature is below or equal to 150 °C.

There existed two interesting features in morphologies among $RuO_2/(Ru + Ir)O_2$ prepared by a sol–gel process (with annealing) [11,12], $RuO_2/(Ru + Ir)O_2$ prepared by dip coating (i.e. thermal decomposition of chloride precursors) [13–15] and $RuO_x{\cdot}nH_2O/(Ru + Ir)O_y{\cdot}mH_2O$ deposits annealed at 200 °C from a comparison of their SEM photographs. First, oxides fabricated by a sol–gel process are, in general, highly porous without any macro or microcracks [11,12]. The vaporization of solvents and thermal decomposition of the chloride precursors in the dip coating method caused the porous morphologies of $RuO_2/(Ru + Ir)O_2$ with many macrocracks [13–15]. In this work, the vaporization of water molecules, however, renders the microcracked surface of the hydrous oxide deposits. The above results indicate the fact that morphologies of Ru and Ru–Ir oxides are not only dependent upon the annealing temperature but also on the preparation method. Second, the surfaces of $RuO_x{\cdot}nH_2O/(Ru + Ir)O_y{\cdot}mH_2O$ deposits annealed at 200 °C show the spherical grains, which are very similar to the morphologies of RuO_2 and Ru (80%) + Ir (20%) oxide prepared by the sol–gel process [11,12], implying the similar EC properties. This speculation is further supported by that the atomic ratio of Ru and Ir in a $(Ru + Ir)O_y{\cdot}mH_2O$ deposit is about 1:10 (Table 1), which is between RuO_2 and Ru (80%) + Ir (20%) oxide. Since all $RuO_x{\cdot}nH_2O/(Ru + Ir)O_y{\cdot}mH_2O$ deposits with annealing are thin and porous, it is predictable that the contribution of the inner electroactive surface sites on the capacitance of hydrous oxides should be minor, which was clearly found for the oxides prepared by dip coating [16].

The surface composition of $(Ru + Ir)O_y{\cdot}mH_2O$ deposits annealed at various temperatures measured by XPS is shown in Table 1. At the annealing temperatures below or equal to 200 °C, the surface composition of this deposit for O, Ru, Ir, Ti and Cl ranges from 55.7 to 59.5, 31.2 to 33.1, 3.3 to 5.6, 0.3 to 0.9 and 4.4 to 7.3 at.%, respectively. Note the significant increase in O and the obvious decrease in Ru when the annealing temperature is equal to or above 250 °C. In addition, the Cl content in the oxide matrix is gradually decreased with increasing the annealing temperature in the whole temperature range of investigation. However, the Ti and Ir contents were not significantly changed with the annealing treatment, indicating the absence of thermal diffusion of Ir and Ti oxides. The surface enrichment of O at the annealing temperature ≥250 °C is attributable to the oxidation of bulk ruthenium metal within the $(Ru + Ir)O_y{\cdot}mH_2O$ deposit since the XRD results in Fig. 1b indicate that ruthenium metal was not obviously oxidized until the annealing temperature is equal to 250 °C. The decrease in Cl with the annealing temperature suggests the replacement of Cl by O during the annealing treatment.

Table 1
Effects of annealing temperatures on surface composition of $(Ru + Ir)O_y{\cdot}mH_2O$ deposits measured by XPS

T_{an} (°C)	O (at.%)	Ru (at.%)	Ir (at.%)	Ti (at.%)	Cl (at.%)
25	55.7	32.8	3.3	0.9	7.3
100	59.5	32.5	3.4	0.6	4.0
150	57.6	31.2	5.6	0.6	5.0
200	58.5	33.1	3.7	0.3	4.4
250	68.3	25.5	3.4	0.2	2.6
300	71.0	24.3	3.9	0.8	0[a]

[a] This element was not found.

3.2. Voltammetric behavior of $RuO_x{\cdot}nH_2O$ and $(Ru + Ir)O_y{\cdot}mH_2O$ in H_2SO_4

In this work, all oxide-coated electrodes were examined by CV since the shapes of cyclic voltammograms can be qualitatively employed as an index in evaluating the ideality of EC characteristics for electroactive materials in the application of EC supercapacitors [1–3]. Typical CV curves measured in 0.5 M H_2SO_4 for $RuO_x{\cdot}nH_2O$ annealed in air for 2 h at 100, 150, 200, 250 and 300 °C are shown as curves 2–6, respectively, in Fig. 3. In addition, the CV curve of the as-prepared $RuO_x{\cdot}nH_2O$ is also shown as curve 1 in this figure. Note that voltammetric currents corresponding to the redox couples in the potential ranges of 0.2–0.8 and 0.8–1.1 V become unclear when this oxide was annealed at temperatures greater than 100 °C. In addition, these peaks disappear at temperatures equal to or above 200 °C. However, the background currents (e.g. curves 4–6) are not seriously changed by the annealing treatment. This is different from the case that a lower loading of $RuO_x{\cdot}nH_2O$ results in lower voltammetric currents within the whole potential region (Fig. 3 in reference [1]). Thus, a rectangular cyclic voltammogram, which is very close to the responses

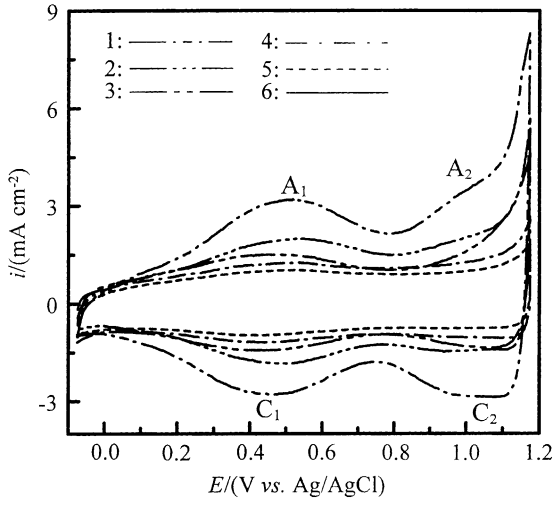

Fig. 3. Voltammetric curves of $RuO_x{\cdot}nH_2O$ annealed in air for 2 h at (1) 25; (2) 100; (3) 150; (4) 200; (5) 250 and (6) 300 °C. CV were measured in 0.5 M H_2SO_4 at 20 mV s^{-1}.

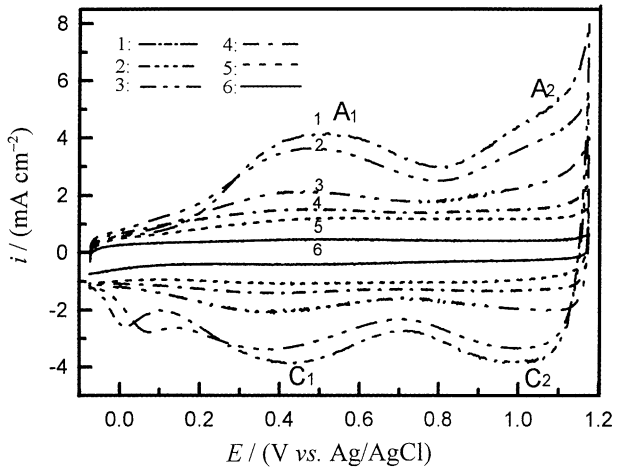

Fig. 4. Voltammetric curves of $(Ru + Ir)O_y{\cdot}mH_2O$ annealed in air for 2 h at (1) 25 °C; (2) 100 °C; (3) 150 °C; (4) 200 °C; (5) 250 °C and (6) 300 °C. CV were measured in 0.5 M H_2SO_4 at 20 mV s^{-1}.

of an ideal capacitor, is found for $RuO_x{\cdot}nH_2O$ annealed at temperatures equal to or above 200 °C. The annealed oxide is therefore considered as a promising electrode material for the application of EC supercapacitors although its voltammetric currents were much lower than that of its unannealed counterpart.

The CV curves measured in 0.5 M H_2SO_4 for $(Ru + Ir)O_y{\cdot}mH_2O$ electrodes annealed in air at 100, 150, 200, 250 and 300 °C, respectively, for 2 h are shown as curves 2–6 in Fig. 4. In addition, voltammetric behavior of the as-prepared $(Ru + Ir)O_y{\cdot}mH_2O$ electrode is also shown as curve 1 in Fig. 4 for comparison purposes. The voltammetric responses of freshly prepared binary oxide (curve 1 in Fig. 4) are very similar in shape to those of freshly prepared $RuO_x{\cdot}nH_2O$ (curve 1 in Fig. 3) while an additional cathodic peak was found at 0 V on the former curve. This additional peak did not disappear until the annealing temperature is equal to or above 150 °C. These results suggest that voltammetric currents were mainly contributed by $RuO_x{\cdot}nH_2O$ although binary oxides have been found to possess much higher specific capacitance [2]. Also note the disappearance of peaks C_1/A_1 and C_2/A_2 when the annealing temperature was above or equal to 200 °C meanwhile an obvious decrease in background currents was found with increasing the annealing temperature. The latter phenomenon is not obvious for the case of $RuO_x{\cdot}nH_2O$ deposits with annealing. Although, the actual reasons responsible for the above difference in background currents are still unclear, it can be reasonably explained by the following. First, the loading of a mixed oxide-coated electrode was about half of a $RuO_x{\cdot}nH_2O$-coated electrode while a freshly prepared binary oxide electrode possessed a larger voltammetric charge (Figs. 3 and 4). This result reveals that the mixing of iridium oxide into the $RuO_x{\cdot}nH_2O$ deposit renders a sharp increase in electroactive nonstoichiometric sites of $RuO_x{\cdot}nH_2O$ deposits since nonstoichiometric sites were believed to exhibit the redox transitions [16–18]. This proposal is further supported by the formation of smaller $(Ru+ Ir)O_y{\cdot}mH_2O$ particles on the binary oxide deposit (Fig. 2). Second, annealing renders a denser deposit and a structural reconstruction for $(Ru + Ir)O_y{\cdot}mH_2O$ (see XRD and SEM results in Figs. 1 and 2). Thus, a loss in nonstoichiometric sites should be very obvious. Since the loading of a binary oxide-coated electrode is much smaller than that of a $RuO_x{\cdot}nH_2O$-coated electrode, a combination of the loss in nonstoichiometric sites and the much smaller loading probably causes the more obvious decrease in background currents for the binary oxide electrode after the annealing treatment.

The effect of annealing temperatures on the voltammetric charges (q^*) of $RuO_x{\cdot}nH_2O$ and $(Ru + Ir)O_y{\cdot}mH_2O$ is shown in Fig. 5 where curves 1 and 2 represent the q^* data for $RuO_x{\cdot}nH_2O$ and $(Ru + Ir)O_y{\cdot}\ mH_2O$, respectively. The voltammetric charge of a freshly prepared $(Ru + Ir)O_y{\cdot}mH_2O$ deposit (120 cycles of CV) is larger than that of a newly prepared $RuO_x{\cdot}nH_2O$ deposit (120 cycles of CV) although the loading of the former deposit is about half of the latter. In addition, the voltammetric charges of both deposits decreased gradually with increasing the annealing temperature, indicating that the vaporization of water, the crystallization and/or the reconstruction of the deposits (Figs. 1 and 2) cause the obvious loss in pseudocapacitance. On the other hand, from a comparison of curves 1 and 2 in Fig. 5, the loss of voltammetric charges (i.e. pseudocapacitance) for $(Ru + Ir)O_y{\cdot}\ mH_2O$ deposits was more obvious than that of $RuO_x{\cdot}nH_2O$. The former result, i.e. a decrease in voltammetric charges for $RuO_x{\cdot}nH_2O$ and $(Ru + Ir)O_y{\cdot}mH_2O$ deposits with annealing, is attributed to the structural reconstruction and/or crystallization of oxide since the nonstoichiometric sites of $RuO_x{\cdot}nH_2O$ and $(Ru + Ir)O_y{\cdot}mH_2O$ deposits are believed to be sharply degraded by the crystallization of ruthenium oxide. Moreover, the reconstruction of $(Ru + Ir)O_y{\cdot}mH_2O$ particles due to the movement of surface Ru/Ir oxides with a lower coordination

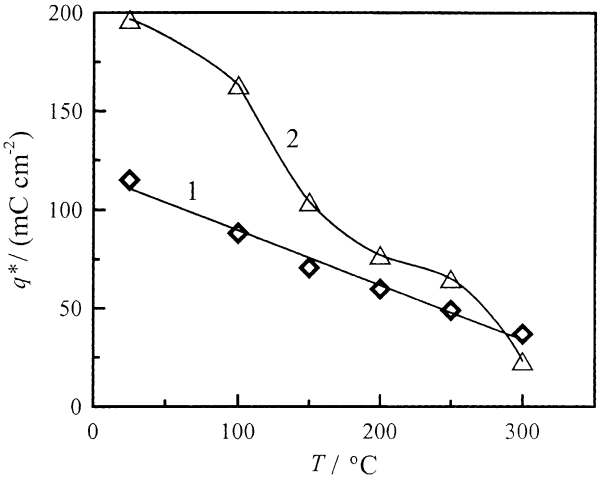

Fig. 5. Effects of annealing temperatures on voltammetric charges of (1) $RuO_x{\cdot}nH_2O$ and (2) $(Ru + Ir)O_y{\cdot}mH_2O$.

number into the energy-favorable sites further supports this opinion. Since the much larger specific pseudocapacitance of binary oxides was attributed to the presence of a higher density of nonstoichiometric sites [2] the above phenomenon further supports the proposal that annealing favors the rearrangement of atoms on the nonstoichiometric sites, resulting in the larger loss of pseudocapacitance for the binary oxides.

From Figs. 3 and 4, rectangular cyclic voltammograms, which were very close to the responses of an ideal capacitor, were found for $RuO_x{\cdot}nH_2O$ and $(Ru + Ir)O_y{\cdot}mH_2O$ when they were annealed at temperatures $\geq$200 °C. In addition, hysteresis in voltammetric responses for $RuO_2{\cdot}nH_2O$ prepared by a sol–gel process [5] became more obvious with increasing the scan rate of CV. Accordingly, the effect of annealing temperature on the EC reversibility of redox transitions for the $RuO_x{\cdot}nH_2O$ and $(Ru + Ir)O_y{\cdot}mH_2O$ deposits is also examined in this work. Typical CV curves measured at different scan rates in 0.5 M H_2SO_4 for the $(Ru + Ir)O_y{\cdot}mH_2O$ deposits annealed in air at 100 and 200 °C for 2 h are shown in Fig. 6a and b, respectively. Note that in both figures, voltammetric currents are gradually increased with the steady increase in scan rate. In addition, voltammetric currents at various potentials are found to be approximately linear with the scan rate of CV. The above result further supports the proposal that the highly rough and microcracked structure of the $RuO_x{\cdot}nH_2O$ and $(Ru + Ir)O_y{\cdot}mH_2O$ with annealing depresses the presence of inner electroactive surface sites. On the other hand, relatively distorted responses (e.g. the negative shift in E_P for the cathodic peak in the hydrogen adsorption region with increasing scan rates) for the $(Ru + Ir)O_y{\cdot}mH_2O$ deposit annealed at 100 °C become more obvious with increasing the scan rate of CV, indicating the hysteresis of the redox transitions on this deposit. From the above results and discussion, hydrous oxides with annealing in air at temperatures $\geq$200 °C exhibit the EC characteristics for an ideal supercapacitor although this treatment causes a significant loss in pseudocapacitance.

3.3. Pseudocapacitance evaluated by CV

$RuO_x{\cdot}nH_2O$ and $(Ru + Ir)O_y{\cdot}mH_2O$ provided several oxidation states to proceed the faradaic redox transitions at the electrode-electrolyte interface in the water decomposition potential window [1,2,16–18]. These transitions include M(III)/M(II), M(IV)/M(III) and M(VI)/M(IV) [16–18] where M indicates both Ru and Ir. Since the voltammetric charge, q^*, (C cm^{-2}) integrated from a cyclic voltammogram has been recognized as an effective index in determining the number of electroactive oxycations involving in the redox transitions [16–18], q^* integrated from −0.05 to 1.15 V on the negative sweeps of CVs is employed to calculate the pseudocapacitance of $RuO_x{\cdot}nH_2O$ and $(Ru+Ir)O_y{\cdot}mH_2O$ deposits with annealing of different temperatures. The mean pseudocapacitance of these oxides can be

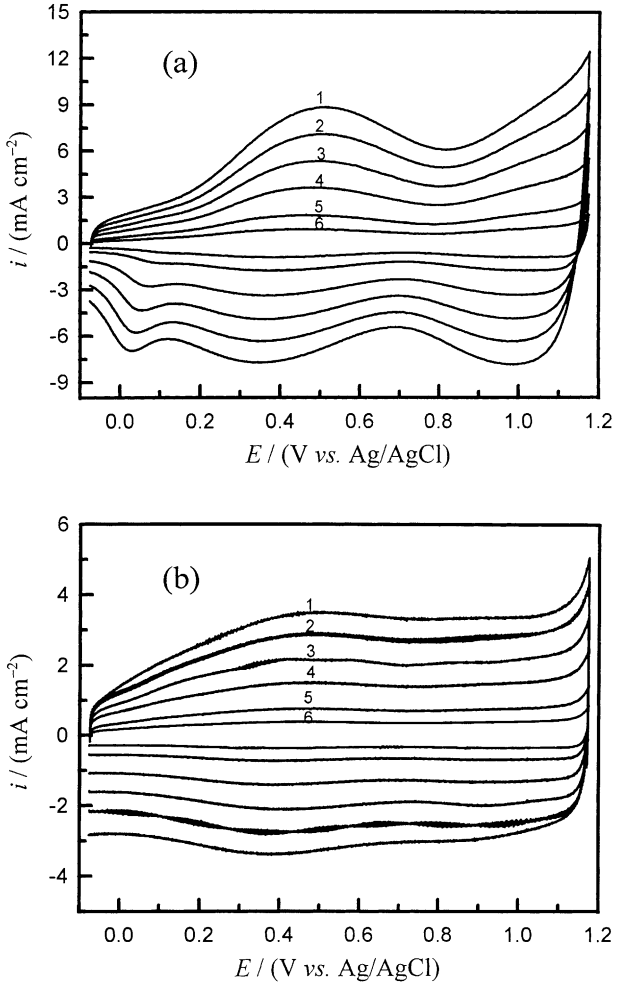

Fig. 6. Voltammetric curves measured at (1) 50 mV s^{-1}; (2) 40 mV s^{-1}; (3) 30 mV s^{-1}; (4) 20 mV s^{-1}; (5) 10 mV s^{-1} and (6) 5 mV s^{-1} in 0.5 M H_2SO_4 for $(Ru + Ir)O_y{\cdot}mH_2O$ deposit annealed in air for 2 h at (a) 100 and (b) 200 °C.

calculated as follows:

$$C_{q^*}(\mathrm{F\,cm^{-2}}) = \frac{\text{voltammetric charges}}{\text{voltage range}} = \frac{q^*}{1.2} \quad (1)$$

In addition, the stability of these oxides can be evaluated by the repeated sweeps of CV measurements in the aqueous media. Typical cyclic voltammograms of the $(Ru + Ir)O_y{\cdot}mH_2O$ deposits annealed in air at 100 and 200 °C for 2 h measured at 20 mV s^{-1} in 0.5 M H_2SO_4 are shown in Fig. 7a and b, respectively. In Fig. 7a, voltammetric currents decrease obviously with increasing the sweep cycles, indicating a significant decay in voltammetric charges for the $(Ru + Ir)O_y{\cdot}mH_2O$ deposits annealed in air at 100 °C. In addition, voltammetric curves of this electrode become asymmetric with increasing the cycle number of CV. These results suggest the instability of this oxide, causing a serious loss in pseudocapacitance. In Fig. 7b, on the other hand, no visible change in voltammetric currents was found, indicating the excellent stability of the $(Ru + Ir)O_y{\cdot}mH_2O$ deposit

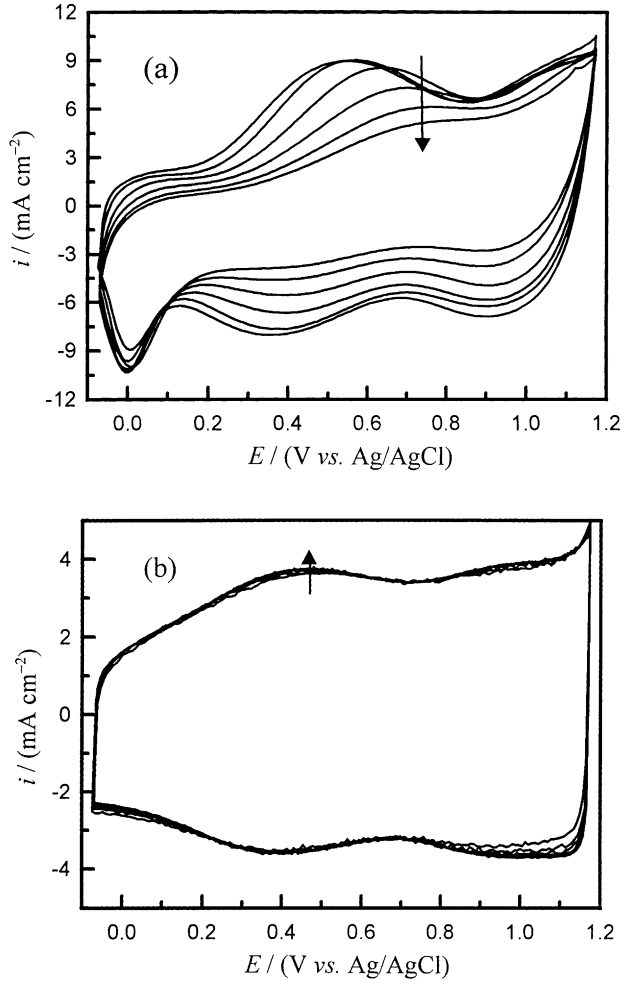

Fig. 7. Cyclic voltammograms of $(Ru + Ir)O_y{\cdot}mH_2O$ annealed in air for 2 h at (a) 100 °C and (b) 200 °C measured at 20 mV s^{-1} in 0.5 M H_2SO_4. The cycle number on these curves with the arrow direction is 5, 20, 40, 60, 80 and 100.

annealed in air at 200 °C. Since similar phenomena were also found for the $RuO_x{\cdot}nH_2O$ deposits with annealing, their cyclic voltammograms are not shown here. From all the above results and discussion, hydrous oxides with annealing in air at temperatures ≥200 °C exhibit not only good EC characteristics but also excellent stability for the EC supercapacitors.

The dependence of pseudocapacitance of $RuO_x{\cdot}nH_2O$ and $(Ru + Ir)O_y{\cdot}mH_2O$ deposits with different annealing temperatures on the CV cycle number is also examined in this work. Typical results measured at 20 mV s^{-1} in 0.5 M H_2SO_4 for the $(Ru + Ir)O_y{\cdot}mH_2O$ deposits annealed in air at 100, 150, 200, 250 and 300 °C for 2 h are shown as curves 2–6 in Fig. 8. In addition, the results for a freshly prepared deposit are also shown as curve 1 in the same figure. Note that on curve 1, mean pseudocapacitance decreases exponentially from 0.146 to 0.023 F cm^{-2} with increasing the CV cycles, indicating the intrinsic instability of hydrous oxides during potential cycling. On curve 2, mean pseudocapacitance of the $(Ru + Ir)O_y{\cdot}mH_2O$ deposit annealed in air for 2 h at

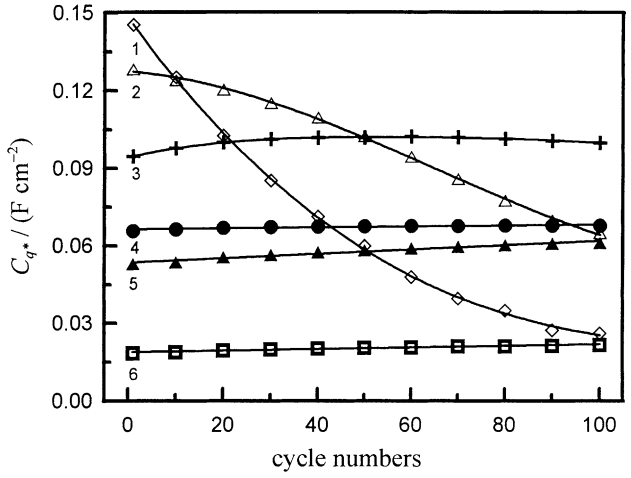

Fig. 8. Effects of annealing temperatures on the mean pseudocapacitance of $(Ru + Ir)O_y{\cdot}mH_2O$ annealed in air for 2 h at (1) 25; (2) 100; (3) 150; (4) 200; (5) 250 and (6) 300 °C. Cyclic voltammograms were measured at 20 mV s^{-1} in 0.5 M H_2SO_4.

100 °C decays gradually from 1 to 30 cycles and then decreases more quickly and linearly with increasing the CV cycles. On the other hand, when the annealing temperature is equal to 150 °C, mean pseudocapacitance reaches a maximum as the CV cycle number is equal to ca. 60 and then decays very slowly in the following sweeps. Moreover, when the annealing temperatures is equal to or above 200 °C, mean pseudocapacitance of $(Ru + Ir)O_y{\cdot}mH_2O$ deposits increases monotonously with the cycle number of CV. These results imply that the vaporization of water molecules and the reconstruction of $(Ru + Ir)O_y{\cdot}mH_2O$ promote its EC stability since the activation energy of $(Ru + Ir)O_y{\cdot}mH_2O$ dissolution should be increased by the reorganization of hydrous oxides from a metastable state to an energy-favorable state through means of annealing [19].

3.4. Pseudocapacitance evaluated by chronopotentiometry

The performance of an electroactive material for the EC supercapacitors was proposed to examine its charging and discharging behavior through means of chronopotentiometry and $i/(dV/dt)$ from the chronopotentiograms can be used to evaluate the pseudocapacitance [1–3]. In this work, the average pseudocapacitance of $RuO_x{\cdot}nH_2O$ and $(Ru + Ir)O_y{\cdot}mH_2O$ deposits was calculated on the basis of the following equation:

$$C_{cp}(\text{average pseudocapacitance}) = \frac{i}{dV/dt} \approx \frac{i}{DV/Dt}. \quad (2)$$

The charging and discharging behavior of $RuO_x{\cdot}nH_2O$ and $(Ru + Ir)O_y{\cdot}mH_2O$ deposits annealed at different temperatures were examined by chronopotentiometry. Typical chronopotentiograms, measured between 0 and 1.15 V in a 0.5 M H_2SO_4 solution at 100 μA cm^{-2}, for $RuO_x{\cdot}nH_2O$ deposits annealed at 100, 150, 200, 250 and 300 °C, respec-

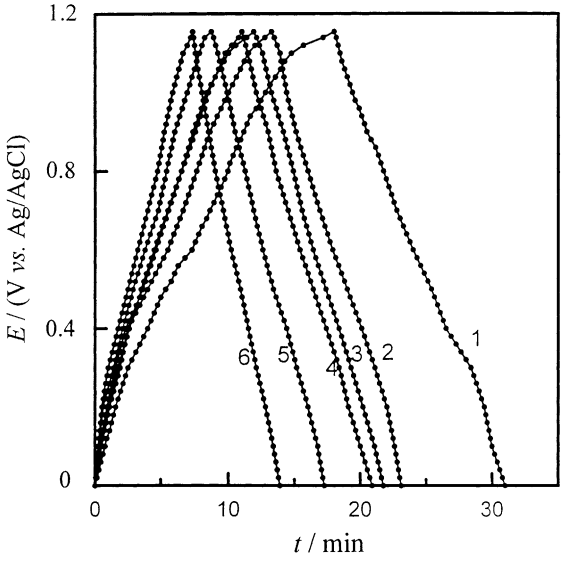

Fig. 9. Chronopotentiograms of $RuO_x{\cdot}nH_2O$ annealed at (1) 25; (2) 100; (3) 150; (4) 200; (5) 250 and (6) 300 °C. These curves were measured between 0 and 1150 mV in 0.5 M H_2SO_4 at 100 μA cm^{-2}.

tively, shown as curves 2–6 in Fig. 9. In addition, the result for the as-prepared oxide is also shown as curve 1 in Fig. 9. Note that the charging–discharging diagrams of $(Ru + Ir)O_y{\cdot}mH_2O$ deposits annealed at different temperatures are very similar to those shown in Fig. 9, their chronopotentiograms are thus not shown in this paper. On curve 1 in Fig. 9, the slopes (dV/dt) of both charging and discharging curves are potential-dependent, indicating the intrinsic EC reversibility of the redox couples within $RuO_x{\cdot}nH_2O$. In addition, from a comparison of curves 1–6, the absolute values of their slopes increase with increasing the annealing temperature, indicating that charges or energies stored in the oxide deposits are decreased with the gradual increase in annealing temperatures. On the other hand, these slopes become potential-independent with increasing the annealing temperature, revealing the change in EC characteristics of the redox couples within the hydrous oxide deposit through means of annealing. Since the slope of charging–discharging plots for an ideal capacitor has to be potential-independent and maintains constant at a specified current density, the charging–discharging performance of $RuO_x{\cdot}nH_2O$, grown by CV, has been improved by annealing at temperatures equal to or above 200 °C.

Effects of annealing temperatures on the performance (i.e. q^*, slope of $1/q^*$ against $v^{1/2}$, mean pseudocapacitance (C_{q^*}) from CV, average pseudocapacitance (C_{cp}) from chronopotentiometry and capacitance ratio (C_{cp}/C_{q^*})) of $RuO_x{\cdot}nH_2O$ and $(Ru + Ir)O_y{\cdot}mH_2O$ deposits are shown in Table 2 for the purpose of convenient comparisons. In addition, the relative loading and specific capacitance of these deposits were also shown in this table. Note that the oxide loading on the freshly prepared electrodes of the same oxide is different from each other. The maximal deviation is about ±10% of the oxide loading, which is larger than the absolute weight difference between the electrodes of the same oxide with different annealing temperatures. Thus, effects of the annealing temperature on the loading were expressed in terms of the relative loading (i.e. the loading ratio of the electrode before and after annealing; see the third column in Table 2). Note that the relative loading of oxide decreased monotonously with increasing the annealing temperature while the loading increased when the annealing temperature was equal to or above 300 and 250 °C for $RuO_x{\cdot}nH_2O$ and $(Ru + Ir)O_y{\cdot}mH_2O$ deposits, respectively. The decrease in loading indicates the vaporization of water molecules trapped within the oxide matrix while the increase in loading at higher temperatures is attributable to the oxidation of bulk Ru and inner-layer Ti metals. Voltammetric charges of $RuO_x{\cdot}nH_2O$ and $(Ru + Ir)O_y{\cdot}mH_2O$ deposits, q^* shown in the fourth column, decreased monotonously with increasing the annealing temperature, indicating that the vaporization of water molecules trapped within the oxide matrix

Table 2
Effects of annealing temperatures on EC characteristics of $RuO_x{\cdot}nH_2O$ and $(Ru + Ir)O_y{\cdot}mH_2O$

Oxides	T_{an} (°C)	Loading (%)[a]	q^* (mC cm^{-2})	S[b]	C_{cp} (mF cm^{-2})	C_{cp}/C_{q^*}	C_S (F g^{-1})
$RuO_x{\cdot}nH_2O$	RT[c]	100	115.0	0.044	98.7	1.03	105.1
	100	94.2	88.3	0.083	67.4	1.08	76.3
	150	88.3	70.8	0.111	62.1	1.10	74.9
	200	86.8	59.8	0.115	58.8	1.17	72.3
	250	84.5	49.0	0.135	48.2	1.22	61.7
	300	84.7	36.9	0.153	38.6	1.26	48.9
$(Ru+Ir)O_y{\cdot}mH_2O$	RT	100	196.7	0.019	165.4	1.01	367.6
	100	92.4	163.4	0.030	138.7	1.02	333.4
	150	86.3	104.1	0.032	91.4	1.05	235.1
	200	83.7	77.3	0.056	69.0	1.07	183.2
	250	84.3	65.3	0.066	60.4	1.11	159.1
	300	84.9	23.2	0.103	20.6	1.17	54.7

[a] The relative loading of oxides, the average loading of $RuO_x{\cdot}nH_2O$ and $Ru + Ir)O_y{\cdot}mH_2O$ is 9.4×10^{-4} and 4.5×10^{-4} g, respectively.
[b] S: slope of $1/q^*$ against the square root of scan rate, $v^{1/2}$.
[c] RT ≈25 °C.

as well as the reconstruction of oxides render the loss in electroactive sites. The presence of so-called ''inner'' and ''outer'' active surface areas on the oxide-coated electrodes is distinguishable by studying the dependence of $1/q^*$ on the square root of scan rates ($v^{1/2}$) of CV in an inert electrolyte [1,16]. The results for the slopes (i.e. S) of $1/q^*$ against $v^{1/2}$for these oxide deposits are shown in the fifth column in Table 2. For all oxide deposits, there existed an approximately linear dependence between $1/q^*$ and $v^{1/2}$. In addition, S values increased gradually with increasing the annealing temperature, especially for the $RuO_x{\cdot}nH_2O$ deposit. These results indicate the presence of ''inner'' electroactive surface area, attributable to the denser structures of $RuO_x{\cdot}nH_2O$ and $(Ru + Ir)O_y{\cdot}mH_2O$ deposits annealed at a higher temperature. Since the diffusion path of proton should be shorter for the oxide deposits with a lower loading, smaller S values for the $(Ru + Ir)O_y{\cdot}mH_2O$ deposits are understandable. Although the increase in S is significant, the redox couples on/within both $RuO_x{\cdot}nH_2O$ and $(Ru + Ir)O_y{\cdot}mH_2O$ deposits with annealing still exhibit reversible properties from the results of voltammetric and chronopotentiometric measurements (Figs. 3–9). In addition, their slopes are much smaller that of the thermally prepared oxides [16]. Therefore, the contribution of the inner electroactive surface sites on the voltammetric charges of hydrous oxides with annealing is minor in comparison with the thermally prepared oxides. In the sixth column, the dependence of C_{cp} on the annealing temperature is very similar in trend to that of q^* from CV while pseudocapacitance of the same electrode obtained by chronopotentiometry is larger than that measured by CV (C_{cp}/C_{q^*} in the seventh column). Since the dc current density employed in chronopotentiometry is very low (100 μA cm^{-2}), charging and discharging processes are believed to perform under a condition close to the quasi-equilibrium state. Pseudocapacitance of the same electrode measured by chronopotentiometry at a very low current density should be larger than that obtained by CV at a moderate scan rate (i.e. 20 mV s^{-1}). Note that the C_{cp}/C_{q^*} ratio also increased gradually with increasing the annealing temperature. This result also supports the presence of ''inner'' electroactive surface area (although its effect is minor) due to the reconstruction of oxides since a denser structure should enlarge the barrier of proton diffusion during the redox transitions. The specific capacitance of all oxides prepared in this work was also shown in Table 2 (the eighth column). Note that the specific capacitance of $RuO_x{\cdot}nH_2O$ decreased gradually and monotonously from 105 to 49 F g^{-1} with increasing the annealing temperature. However, a more sharp decrease in specific capacitance from 368 to 55 F g^{-1} was found for the $(Ru + Ir)O_y{\cdot}mH_2O$ deposits with increasing the annealing temperature. The above results also supported the statement that annealing rendered the vaporization of trapped water, crystallization/reconstruction of hydrous oxides and oxidation of bulk Ru metal, resulting in the loss of nonstoichiometric sites for the pseudocapacitance.

4. Conclusions

On the basis of XRD spectra and XPS data, the as-prepared $RuO_x{\cdot}nH_2O$ and $(Ru + Ir)O_y{\cdot}mH_2O$ should consist of a mixture of Ru species with various oxidation states, including Ru metal. This metal was oxidized/converted into RuO_2 at annealing temperatures equal to/above 200 °C while this bulk oxidation of ruthenium metal within $(Ru+Ir)O_y{\cdot}mH_2O$ occurred at the annealing temperature equal to/above 250 °C. The vaporization of trapped water molecules favored the crystallization of RuO_2 at annealing temperature equal to/above 100 °C on a $RuO_x{\cdot}nH_2O$ deposit while the presence of iridium in the oxide inhibited the crystallization of RuO_2 at annealing temperature equal to 300 °C. Due to the annealing treatment, vaporization of trapped water and crystallization/reconstruction of $RuO_x{\cdot}nH_2O$ and $(Ru + Ir)O_y{\cdot}mH_2O$ caused an obvious loss in pseudocapacitance. These oxide deposits with annealing in air for 2 h at temperatures equal to/above 200 °C exhibited the EC characteristics very close to an ideal capacitor. The annealing treatment also promoted the stability of these oxides, due to the formation of a denser and more ordered/organized structure.

Acknowledgements

The financial support of this work, by the National Science Council of the Republic of China under contract no. NSC 90-2214-E-194-007, is gratefully acknowledged.

References

[1] C.-C. Hu, Y.-H. Huang, J. Electrochem. Soc. 146 (1999) 2465 and references cited therein.
[2] C.-C. Hu, K.-H. Chang, Electrochim. Acta 45 (2000) 2685 and references cited therein.
[3] C.-C. Hu, C.-H. Chu, Mat. Chem. Phys. 65 (2000) 329.
[4] S. Sarangapani, B.V. Tilak, C.-P. Chen, J. Electrochem. Soc. 143 (1996) 3791.
[5] J.P. Zheng, P.-J. Cygon, T.R. Jow, J. Electrochem. Soc. 142 (1995) 2699.
[6] Y. Sato, K. Yomogida, T. Nanaumi, K. Kobayakawa, Y. Ohsawa, M. Kawai, Electrochem. Solid-State Lett. 3 (2000) 113.
[7] F. Fusalba, H.A. Ho, L. Breau, D. Bélanger, Chem. Mater. 12 (2000) 2581.
[8] B.E. Conway, Electrochemical Supercapacitors, Kluwer-Plenum Pub. Co., New York, 1999.
[9] S. Hadzi-Jordanov, H. Angerstein-Kozlowska, M. Vukovic, B.E. Conway, J. Electrochem. Soc. 125 (1978) 1471.
[10] C.-C. Hu, C.-Y. Lin, T.-C. Wen, Mat. Chem. Phys. 44 (1996) 233.
[11] Y. Murakami, K. Miwa, M. Ueno, M. Ito, K. Yahikozawa, Y. Takasu, J. Electrochem. Soc. 141 (1994) L118.
[12] M. Ito, Y. Murakami, H. Kaji, H. Ohkawauchi, K. Yahikozawa, Y. Takasu, J. Electrochem. Soc. 141 (1994) 1243.
[13] S.-M. Lin, T.-C. Wen, J. Electrochem. Soc. 140 (1993) 2265.
[14] K. Kameyama, K. Tsukada, K. Yahikozawa, Y. Takasu, J. Electrochem. Soc. 141 (1994) 643.

[15] C.-C. Hu, C.-H. Lee, T.-C. Wen, J. Appl. Electrochem. 26 (1996) 72.
[16] S. Trasatti, Electrochim. Acta 36 (1991) 225.
[17] T.-C. Wen, C.-C. Hu, J. Electrochem. Soc. 139 (1992) 2158.
[18] Electrodes of Conductive Metallic Oxides. Parts A and B, in: S. Trasatti (Ed.), Elsevier, Amsterdam, 1981.
[19] C.-C. Hu, K.-Y. Liu, Electrochim. Acta 45 (2000) 3063.